THE JOURNAL OF PHYSICAL CHEMISTRY C
A JOURNAL OF THE AMERICAN CHEMICAL SOCIETY

pubs.acs.org/JPCC
Article

Exploring the Halide Exchange Engineering on Lead-free $Cs_2AgSbCl_{6-\delta}Br_\delta$ Mixed-Halide Double Perovskite: A DFT Study

José A. S. Laranjeira, Sérgio A. Azevedo, Felipe A. La Porta, Mateus M. Ferrer, Elson Longo, and Julio R. Sambrano*

Cite This: J. Phys. Chem. C 2024, 128, 11858−11869

Read Online

ACCESS | Metrics & More | Article Recommendations | Supporting Information

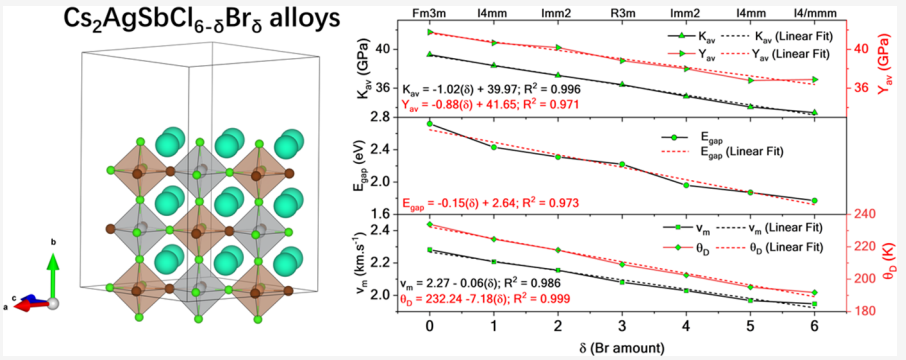

ABSTRACT: Halide perovskites, commonly studied in optoelectronics, have an ABX_3 structure, where A^+ is a monovalent cation, B^{2+} is a divalent cation, and X^- is a halide ion. The use of the Pb^{2+} ion in the B site has generated some concern regarding its toxicity in a possible large-scale application. To address this, replacing Pb^{2+} with heterovalent elements is explored to obtain double halide perovskites, denoted as $A_2B'B''X_6$, where B′ and B″ are trivalent and monovalent cations, respectively. Anion exchange reactions can tailor the optical and electronic properties of these structures by band gap energy control. This study seeks to reveal the strong correlation between the structure composition of $Cs2AgSbCl_{6-\delta}Br_\delta$ mixed-halide double perovskites by means of computational simulations. These structures consist of three-dimensional (3D) lattices of $[SbCl_{6-\delta}Br_\delta]$ and $[AgCl_{6-\delta}Br_\delta]$ distorted octahedral clusters. For different δ values, the compounds exhibit different space groups: $I4mm$ (C_{4v}) for $\delta = 2$ and 4, remaining $I4mm$ (C_{4v}) for $\delta = 1$ and 5, and showing $R3m$ (C_{3v}) symmetry for $\delta = 3$. Incorporating Br^- significantly reduces structural organization in short and long ranges. All $Cs_2AgSbCl_{6-\delta}Br_\delta$ compounds exhibit indirect band gap energy at the $X \rightarrow L$ point, reducing from 2.72 to 1.77 eV with the increased Br content.

1. INTRODUCTION

In recent years, solar energy has emerged as a promising alternative to conventional fossil fuels, offering a sustainable and inexhaustible energy source.[1] This development has spurred advancements in photovoltaic technology aimed at efficiently harnessing the solar energy spectrum within economically viable and environmentally sustainable systems.[2,3] Although silicon-based solar cells contributed to the early development of solar energy, they are still considered relatively inefficient due to production problems and inefficiency in the energy conversion rate.[4,5] Consequently, there has been a growing effort to explore alternative novel photovoltaic materials that are cost-competitive and environmentally friendly.[6−8] The efficiency of perovskite-based solar modules has increased significantly in the past decade (i.e., with an area up to 0.1 cm^2), which in 2009 was ∼3.8% and in 2021 ∼25.7%.[9,10]

One of the most promising compounds commonly studied in optoelectronic applications are halide perovskites ABX_3,[1111] where A^+ represents a monovalent cation (which can be a monovalent metal or an organic molecule), B^{2+} is a divalent cation, and X^- a halide (such as Cl^-, Br^-, or I^-).[12] The most reported halide perovskites have Pb^{2+} ions occupying the B site, but Pb-based solar cells present challenges related to stability and toxicity.[13−15] Therefore, the Pb^{2+} replacement with homovalent elements (e.g., Sn, Ge, and others) and heterovalent elements (such as Bi^{3+}, Sb^{3+}, In^{3+}, Ag^+, and Cu^+),[16−20] with general formula $A_2B'B''X_6$, where B′ are trivalent and B″ monovalent cations, respectively, has been investigated.[20] $A_2B'B''X_6$ perovskites are also known as

Received: March 27, 2024
Revised: June 11, 2024
Accepted: June 25, 2024
Published: July 5, 2024

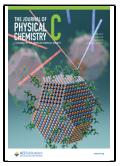

"elpasolite," named after the mineral K_2NaAlF_6.[2121] The ABX_3 and $A_2B'B''X_6$ halide perovskites structures and their representative octahedra are represented in Figure 1. The

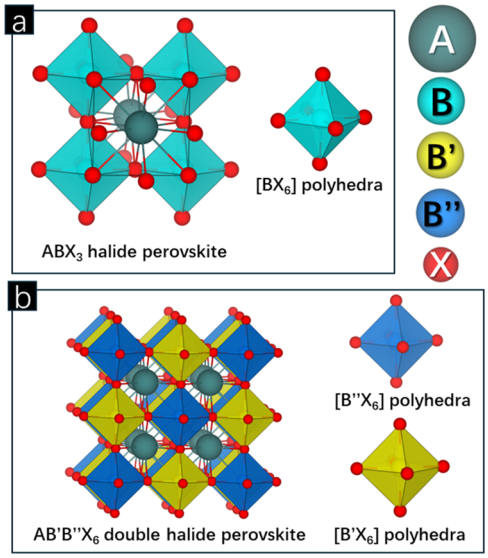

Figure 1. ABX_3 cubic halide perovskite (a) and $AB'B''X_6$ cubic double halide perovskite (b), along with their representative octahedra.

cubic ABX_3 perovskite comprises a three-dimensional lattice of corner-sharing $[BX_6]^{-4}$ octahedra with the A^+ cations located within the interstices formed by these clusters. Meanwhile, the $A_2B'B''X_6$ perovskite possesses an analog structure but exhibits two different alternating $[B'X_6]^{3-}$ and $[B''X_6]^{5-}$ octahedra.

Due to its highest stability, the double halide perovskites class (e.g., $Cs_2AgBiBr_6$, $Cs_2AgSbCl_6$, and $Cs_2AgInCl_6$) has recently been easily synthesized from different methods with pronounced potential for many emerging optoelectronic applications.[22−25] In this sense, McClure et al.[26] obtained $Cs_2AgBiBr_6$ and $Cs_2AgBiCl_6$ with promising band gap energies of 2.19 and 2.77 eV, respectively, and superior moisture stability than $CH_3NH_3PbX_3$. Particularly concerning the $Cs_2AgSbCl_6$, Zhou et al.[27] observed that this material possesses a high decomposition temperature and is stable upon prolonged exposure to air and moisture. Deng et al.[28] showed via theory and experimental collaborative approach that $Cs_2AgSbCl_6$ would be a promising light-absorbing material in contact with anatase TiO_2. On the other hand, Yu et al.[29] revealed the excellent photoelectric performance for Cu-modulated $Cs_2AgSbCl_6$ systems, with the increase of Cu lead in a band gap decrease due to the extra interactions between the Cu 3d orbitals.

Modifying the band gap energy of lead-free double halide perovskites to tailor their optical and electronic properties can be achieved through anion exchange reactions. This cost-effective method involves varying the amounts of Cl^-, Br^-, and I^- ions during synthesis.[30] Such exchanges can affect the electronic structure,[31] charge carrier mobility,[32] and light absorption.[33] Akkerman et al.[34] demonstrated through controlled anion exchange reactions that it is possible to tune the chemical composition and optical properties of $CsPbBr_3$ nanocrystals precisely. Similarly, Wu et al.,[35] employing halide exchange on solid thin films, obtained mixed-halide double perovskites, $Cs_2AgBiBr_{6-x}I_x$, with tunable band gap energy as a function of I^- concentration. Su et al.[36] and Wanniarachchi et al.[37] have explored the anion exchange in $Cs_2AgBiX'_{6-\delta}X''_{\delta}$ (X′ and X″ denoting different halides) alloys via computational simulations and revealed that these systems have an indirect band gap transition regardless of the halide substitution and concentration.

Motivated by the promising properties of lead-free double halide perovskites and the lack of anion exchange studies on $Cs_2AgSbCl_6$, this article offers a comprehensive analysis of the electronic structure and long-range and short-range order characterization of $Cs_2AgSbCl_{6-\delta}Br_{\delta}$ alloys (with δ = 0, 1, 2, 3, 4, 5 or 6) structures via periodic density functional theory (DFT) simulations. The anion exchange effect in these structures makes it possible to design and direct the synthesis of lead-free double halide perovskites with specific characteristics adapted for emerging optoelectronic technologies.

2. METHODOLOGY

The modeling and computational simulations were performed by means of the CRYSTAL17[38] package program under the DFT/PBESOL0 functional[39] with triple-zeta-valence with polarization (TZVP)[40] basis sets to describe the Cs, Ag, Sb, Cl, and Br atomic centers. The precision of the convergence criteria for bielectronic integrals was controlled by a set of five thresholds (10^{-8}, 10^{-8}, 10^{-8}, 10^{-8}, 10^{-16}) that represent the overlap and penetration for Coulomb integrals, the overlap for HF exchange integrals, and the pseudo-overlap, respectively. The reciprocal space was sampled with a shrinking factor of 12. Optimization convergence was monitored using root-mean-square (RMS) and the absolute value of the largest component of both the gradients and the estimated displacements. Hence, the convergence criteria employed for RMS and the largest component for gradient and displacement were 0.00030 and 0.00045 au, and 0.00120 and 0.00180 u.a., respectively. Then, the lattice parameters and atomic positions obtained from the optimized structure were used in the VESTA software[41] for conducting powder X-ray diffraction (XRD) simulations. The band structure and density of states (DOS) of $Cs_2AgSbCl_{6-\delta}Br_{\delta}$ (δ = 0, 1, 2, 3, 4, 5 or 6) were analyzed using the same *k*-point sampling employed for the diagonalization of the Fock matrix in the optimization process along the high-symmetry Brillouin Zone path. Raman intensities were computed using solutions of first and second-order coupled perturbed Hartree−Fock/Kohn−Sham (CPHF/KS) self-consistent equations.[48,49]

3. RESULTS AND DISCUSSION

The cubic unit cell structure of $Cs_2AgSbCl_6$ belongs to $Fm\bar{3}m$ space group (no. 225), and the crystallographic information was extracted from experimental data ($a = b = c$ = 10.557 Å).[42−45] After structural optimization, it was observed that the calculated lattice parameters $a = b = c$ = 10.560 Å agreed with the average experimental value, whose difference is only 1.22%. Concerning band gap energy (E_{gap}), the calculated value is 2.72 eV, a difference of 1.21% from the experimental values (2.69 eV).[42−45]

The relative positions of Br in $Cs_2AgSbCl_{6-\delta}Br_{\delta}$ systems were analyzed to determine the most stable structural arrangement. In this approach, 1, 2, 2, 2, and 1 different nonequivalent positions for δ = 1, 2, 3, 4, and 5 were considered, respectively, as demonstrated in Figure 2. For δ = 1 or 5 (Figure 2a,b, respectively), only one possible non-equivalent configuration was obtained; for δ = 2 or 4 (Figure

https://doi.org/10.1021/acs.jpcc.4c01990
J. Phys. Chem. C 2024, 128, 11858−11869

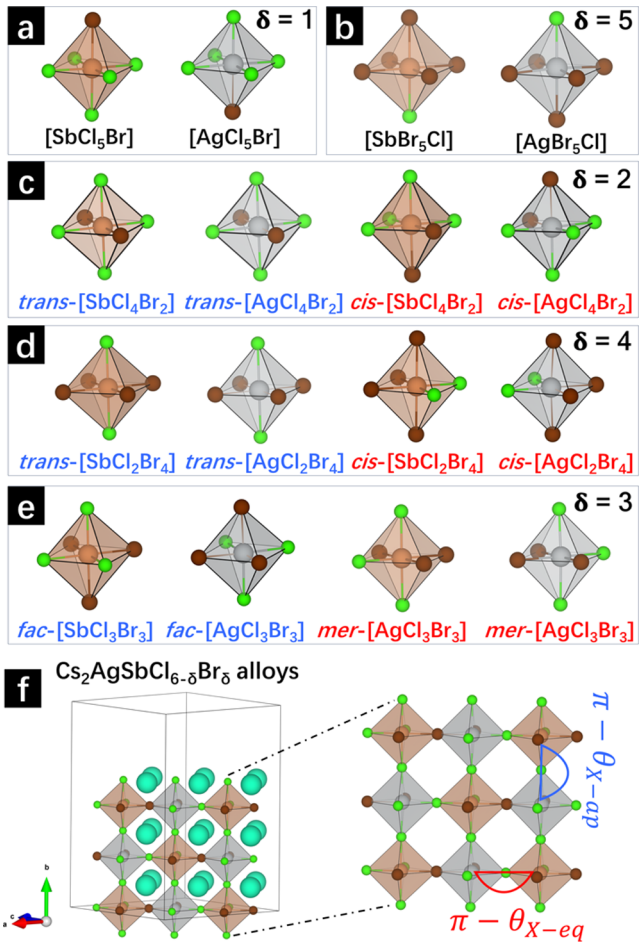

Figure 2. Nonequivalent cluster configurations within $Cs_2AgSbCl_{6-\delta}Br_\delta$ alloys are depicted. They include the $Cs_2AgSbCl_5Br$ (a), $Cs_2AgSbClBr_5$ (b), $Cs_2AgSbCl_4Br_2$ (c), $Cs_2AgSbCl_2Br_4$ (d), and $Cs_2AgSbCl_3Br_3$ (e) systems. Additionally, the generic representation illustrates the relative rotations between neighboring octahedra, which are characterized by $\pi-\theta_{X\text{-}eq}$ and $\pi-\theta_{X\text{-}ap}$ (X = Cl or Br) of these alloys (f).

2c,d, respectively), two nonequivalent arranges can be noted, where the Br or (Cl, for $\delta = 4$) can be disposed in two *cis* or *trans* isomers. Considering $\delta = 3$, two nonequivalent configurations were evaluated, with three Br atoms in the plane (Figure 2e) or two Br atoms in the plane and the third in the axis, equivalent to *meridional* and *facial* isomers, respectively.

The relative stability of the $Cs_2AgSbCl_{6-\delta}Br_\delta$ systems was evaluated in terms of cohesive (E_{coh}) and excess (E_{exc}) energies, as seen in Table 2. Particularly, the E_{coh} refers to the energy required to completely separate a solid into its isolated constituent atoms, accounting for the interactions between the atoms within the solid and is expressed by the equation[46,47]

$$E_{coh} = \frac{1}{N}[E_{Cs_2AgSbCl_{6-\delta}Br_\delta} - (2E_{Cs} + E_{Ag} + E_{Sb} + (6-\delta)E_{Cl} + \delta E_{Br})] \quad (1)$$

where N is the number of atoms in the unit cell, $E_{Cs_2AgSbCl_{6-\delta}Br_\delta}$ is the energy of $Cs_2AgSbCl_{6-\delta}X_\delta$ systems, and E_{Cs}, E_{Ag}, E_{Sb}, E_{Cl}, and E_{Br} denote the energies of isolated Cs, Ag, Sb, Cl, and Br atoms, respectively.

The excess energy (E_{exc}) is a function of the composition, which measures the relative stability of the alloys compared to that of the pure components ($\delta = 0$ and 6). The $E_{exc}(\delta)$ can be obtained from the following equation[48]

$$E_{exc}(\delta) = 6E_{Cs_2AgSbCl_{6-\delta}Br_\delta} - \delta E_{Cs_2AgSbBr_6} - (6-\delta)E_{Cs_2AgSbCl_6} \quad (2)$$

where the $E_{Cs_2AgSbCl_6}$ and $E_{Cs_2AgSbBr_6}$ represent the energy of $Cs_2AgSbCl_6$ and $Cs_2AgSbBr_6$, respectively. These two methods, in general, are used to assess the energetic cost of obtaining $Cs_2AgSbCl_{6-\delta}Br_\delta$ alloys and their stability.

To obtain data concerning the spatial arrangement of octahedra in the lattice, measuring the apical and equatorial ⟨X−B̂−X⟩ angles can be helpful in measuring the polyhedra rotation.[49] For the Cs_2AgSbX_6 (X = Cl or Br) halide double perovskite, these distortions can be described by apical (⟨Sb−X̂−Ag⟩$_{ap}$ or ⟨X⟩$_{ap}$) and equatorial (⟨Sb−X̂−Ag⟩$_{eq}$ or ⟨X⟩$_{eq}$) angles (Figure 2f). The E_{coh}, E_{exc}, and the ⟨Br⟩$_{eq}$, ⟨Br⟩$_{ap}$, ⟨Cl⟩$_{eq}$, and ⟨Cl⟩$_{ap}$ bond angles for $Cs_2AgSbCl_{6-\delta}Br_\delta$ alloys are summarized in Table 1.

Table 1. Cohesive Energy (E_{coh}) in eV/atom, Excess Energy (E_{exc}) in eV, and Sb − $\widehat{Br}$ − Ag and Sb − $\widehat{Cl}$ − Ag Apical and Equatorial Bond Angles (⟨Br⟩$_{ap}$, ⟨Br⟩$_{eq}$, ⟨Cl⟩$_{ap}$, and ⟨Cl⟩$_{eq}$, Respectively) in (deg)

δ	E_{coh}	E_{exc}	⟨Br⟩$_{eq}$	⟨Cl⟩$_{eq}$	⟨Br⟩$_{ap}$	⟨Cl⟩$_{ap}$
0	−4.436			180.00		180.00
1	−4.391	0.139		179.87	180.00	180.00
2-*cis*	−4.348	0.198	179.29	179.41	179.29	179.41
2-*trans*	−4.347	0.261		180.00	180.00	
3-*fac*	−4.306	0.184	178.67	178.73	178.67	178.73
3-*mer*	−4.305	0.244	178.36	178.81	180.00	180.00
4-*cis*	−4.264	0.174	177.36	178.43	178.65	178.43
4-*trans*	−4.263	0.225	180.00			180.00
5	−4.223	0.097	177.25		177.25	180.00
6	−4.183		180.00		180.00	

It is noticed that E_{coh} increase monotonically with the Br amount, indicating that the Br addition makes the $Cs_2AgSbCl_{6-\delta}Br_\delta$ alloys less stable. In light of the E_{exc} values, the crystallization of $Cs_2AgSbClBr_5$ is more favorable between the alloys, i.e., closest to zero E_{exc}. At the same time, a higher energetic cost to obtain the systems for $\boldsymbol{\delta}$ = 2, 3, and 4 concentrations is noticed (higher E_{exc}). The closer to zero E_{exc} demonstrates that the alloys are reliable compared with their pristine counterparts, although they are not necessarily more stable.

In the pristine Cs_2AgSbX_6 structures, the octahedra do not have a freedom degree to make these relative displacements, i.e., due to the high symmetry of these compounds and the <Sb−X̂−Ag> angles are equal to 180°. However, in $Cs_2AgSbCl_{6-\delta}Br_\delta$ alloys, the anion substitution induces a breakdown in symmetry, allowing for the relative motion of the $[SbCl_{6-\delta}Br_\delta]$ and $[AgCl_{6-\delta}Br_\delta]$ octahedra. For $Cs_2AgSbCl_2Br_4$ and $Cs_2AgSbCl_4Br_2$ alloys, the *trans* isomers do not exhibit rotations, being unstable compared to *cis*. For $Cs_2AgSbCl_3Br_3$, the octahedra rotation is observed in a unique direction for the *meridional* isomer, i.e., only for ⟨X⟩$_{eq}$ angles, which can be a differential to the *facial* where the distortion is observed in both apical and equatorial ⟨X⟩ angles. This study focused on

https://doi.org/10.1021/acs.jpcc.4c01990
J. Phys. Chem. C 2024, 128, 11858−11869

Table 2. Lattice Parameters (a, b, c, α, β, and γ), Space Group (SPG), and Point Group (PG) for $Cs_2AgSbCl_{6-\delta}Br_\delta$ Alloys

	a (Å)	b (Å)	c (Å)	α (deg)	β (deg)	γ (deg)	SPG	PG	t	t'	u
$\delta = 0$	10.557	10.557	10.557	90	90	90	$Fm\bar{3}m$	O_h	0.944	3.802	0.528
$\delta = 1$	7.486	7.486	10.713	90	90	90	$I4mm$	C_{4v}	0.931	3.959	0.487
$\delta = 2$	7.601	10.604	7.596	90	90	90	$Imm2$	C_{2v}	0.921	4.116	0.452
$\delta = 3$	7.618	7.618	18.633	90	90	120	$R3m$	C_{3v}	0.911	4.273	0.422
$\delta = 4$	10.942	7.632	7.627	90	90	90	$Imm2$	C_{2v}	0.901	4.430	0.396
$\delta = 5$	7.756	7.756	10.800	90	90	90	$I4mm$	C_{4v}	0.893	4.587	0.373
$\delta = 6$	7.770	7.770	10.989	90	90	90	$I4/mmm$	D_{4h}	0.886	4.744	0.352

the isomers that presented the closest to zero E_{exc} and lowest E_{coh} values for each $Cs_2AgSbCl_{6-\delta}Br_\delta$ composition.

The calculated lattice parameters (a, b, c, α, β, and γ), space group (SPG), point group (PG) and Goldschmidt's (t) and Bartel (t') tolerance and octahedral (u) factors for the $Cs_2AgSbCl_{6-\delta}Br_\delta$ alloys are described in Table 2. The highest symmetry is observed for the $Cs_2AgSbCl_6$ structure, with the $Fm\bar{3}m$ (O_h) space group. Interestingly, it was expected that $Cs_2AgSbBr_6$ exhibits the same symmetry as $Cs_2AgSbCl_6$. However, a distortion in the bond lengths of the $[SbCl_{6-\delta}Br_\delta]$ and $[AgCl_{6-\delta}Br_\delta]$ polyhedra is observed, i.e., resulting in a flattening of octahedra and reducing the symmetry of this compound to $I4/mmm$ (D_{4h}). While this distortion is almost insignificant from a structural point of view, the literature often reports this structure as cubic with the $Fm\bar{3}m$ (O_h) space group.[50,51] Nevertheless, this minor distortion leads to a reduction in the symmetry operations and therefore in the vibrational active modes, as can be displayed in the vibrational analysis. A correspondence between $\delta = 2$ and 4, and for $\delta = 1$ and 5 with the $Imm2$ (C_{2v}) and $I4mm$ (C_{4v}) space groups, respectively, can be observed. Additionally, for $\delta = 3$, the $R3m$ (C_{3v}) symmetry is observed.

Differently reported for simple perovskites (ABX_3) where the Goldschmidt's tolerance factor $t = (r_A + r_X)/\sqrt{2}(r_B + r_X)$, for double halide perovskites, the r_B was obtained as the average value between $r_{Sb^{3+}}$ and r_{Ag^+}. In mixed-anion perovskites, the parameter r_X can be further described using the anionic effective radius (denoted here as $r_{effective}$) which is equal to $(1 - \delta)r_{Cl^-} + \delta r_{Br^-}$, as reported by Siddique et al.[52] to analyze the stability of mixed $CH_3NH_3PbBr_{3-\delta}Cl_\delta$ perovskites. These modifications were also inserted into the calculations of the u and t' factors. t values between 0.75 and 1.00 indicate the formation of perovskite structure.[53] The modified Goldschmidt's (t) and Bartel (t') tolerance and octahedral (u) factors were employed to describe the stability of the perovskite $Cs_2AgSbCl_{6-\delta}Br_\delta$ alloys according to the following expressions

$$t = \frac{r_{Cs^+} + (1 - \delta)r_{Cl^-} + \delta r_{Br^-}}{\sqrt{2}\left[(1 - \delta)r_{Cl^-} + \delta r_{Br^-} + \frac{r_{Sb^{3+}} + r_{Ag^+}}{2}\right]} \quad (3)$$

$$u = \frac{r_{Sb^{3+}} + r_{Ag^+}}{2[(1 - \delta)r_{Cl^-} + \delta r_{Br^-}]} \quad (4)$$

$$t' = \frac{2[(1 - \delta)r_{Cl^-} + \delta r_{Br^-}]}{r_{Sb^{3+}} + r_{Ag^+}} - n_{Cs}\left(n_{Cs} - \frac{2r_{Cs^+}/(r_{Sb^{3+}} + r_{Ag^+})}{\ln[2r_{Cs^+}/(r_{Sb^{3+}} + r_{Ag^+})]}\right) \quad (5)$$

where r_{Cs^+}, r_{Cl^-}, r_{Br^-}, $r_{Sb^{3+}}$, and r_{Ag^+} represent the Cs^+, Cl^-, Br^-, Sb^{3+}, and Ag^+ atomic radii and n_{Cs} denotes the oxidation number of Cs. The atomic radii values were based on the ref 54.

According to Table 2, it is noticed that $0.944 < t < 0.886$ and 0.886, and $0.528 < u < 0.352$, both parameters decreasing with δ increase. On the other hand, more recently, the Bartel tolerance factor (t') was proposed in 2018.[55] In this study, the authors evaluated 576 materials with perovskite structures, achieving a higher accuracy of 92% compared to that of traditional t. It is verified that t' increases with δ and $3.80 < t' < 4.74$. The upper critical value for t' is 4.18, i.e., t' values less than 4.18 indicate stability. This condition is fulfilled only for $\delta = 0$, 1, and 2, which represents a remarkable difference to t, which suggests good stability for all structures. The results highlight that the addition of Br increases the instability in $Cs_2AgSbCl_{6-\delta}Br_\delta$ alloys, with $\delta \geq 3$ tending to be unstable. Finally, the behavior of t and t' corroborates the E_{coh} increase with the Br concentration.

The anion exchange leads to structural distortion in the $[SbCl_{6-\delta}Br_\delta]$ and $[AgCl_{6-\delta}Br_\delta]$ polyhedra. Hence, the effective coordination number (ECoN)[56−59] serves as a valuable metric to characterize these distortions, as depicted in Table 3, which

Table 3. Effective Coordination Number (ECoN), Average Bond Lengths (d_{Ag-Cl}, d_{Ag-Br}, d_{Sb-Cl}, and d_{Sb-Br} in Å) and Volume (V_{Ag} and V_{Sb} in Å^3) for Ag and Sb-Centered Octahedra, Indicated by the Respective Subindexes

	$ECoN_{Sb}$	$ECoN_{Ag}$	d_{Ag-Cl}	d_{Ag-Br}	d_{Sb-Cl}	d_{Sb-Br}
$\delta = 0$	6.00	6.00	2.65		2.63	
$\delta = 1$	5.94	6.00	2.67	2.67	2.63	2.75
$\delta = 2$	5.99	5.90	2.67	2.69	2.63	2.75
$\delta = 3$	5.90	5.99	2.67	2.71	2.64	2.75
$\delta = 4$	5.89	5.98	2.67	2.71	2.64	2.76
$\delta = 5$	5.92	5.98	2.66	2.72	2.63	2.76
$\delta = 6$	6.00	6.00		2.76		2.73

displays the ECoN, the average bond length and volume of Sb and Ag-centered polyhedra. As expected, for $\delta = 0$ or 6, the octahedra do not present distortions. However, for $\delta = 6$, as mentioned before, there are slight distortions that this parameter cannot fully capture. Considering the alloys, notice that, in general, the Sb-centered octahedra are more distorted than Ag, where $\delta = 2$ is the exception. Notably, greater distortion in the $[AgCl_{6-\delta}Br_\delta]$ octahedra is reported for $\delta = 2$, whereas for $[SbCl_{6-\delta}Br_\delta]$, it occurs when $\delta = 4$. Regarding the bond lengths, significant variations were not verified, with the most notable deviations found in d_{Ag-Cl} ($\Delta = 0.30$ Å).

Additionally, it is widely recognized that the positions and intensities of diffraction peaks reveal the arrangement of atoms in the crystal lattice, i.e., thereby elucidating the symmetry and

https://doi.org/10.1021/acs.jpcc.4c01990
J. Phys. Chem. C 2024, 128, 11858−11869

periodicity of the long-range structural organization.[60] In light of this, the XRD patterns were simulated for the $Cs_2AgSbCl_{6-\delta}Br_\delta$ compounds, as depicted in Figure 3a. This

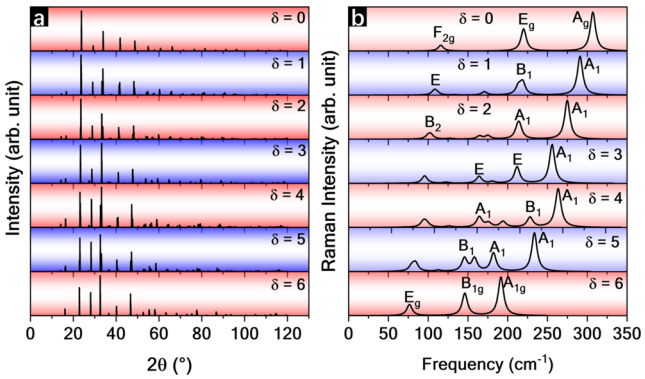

Figure 3. Simulated XRD patterns (a) and Raman spectra of $Cs_2AgSbCl_{6-\delta}Br_\delta$ structures (b).

result shows well-defined XRD peaks are present, i.e., indicating the highest long-range order within these systems. This observation aligns with the analysis presented in Table 2, where it is evident that these systems possess more symmetry operators than solid solutions (consider the space group and point group). As outlined in Table 2, the $\delta = 3$ configuration exhibits enhanced long-range order among the solid solutions, characterized by well-defined peaks.

At a 2Θ angle of approximately 24°, the highest peaks are prominent in Cl-majority systems, while in Br-majority, these peaks shift to 2Θ = 33°. Noteworthy is the equilibrium point where Br and Cl concentrations are equal ($\delta = 3$), resulting in two equal peaks. These observations underscore the utility of XRD analysis in discerning the impact of different compositions on the crystalline arrangement of the $Cs_2AgSbCl_{6-\delta}Br_\delta$ alloys.

The simulated Raman spectra of the $Cs_2AgSbCl_{6-\delta}Br_\delta$ structures are reported in Figure 3b, revealing alterations in short-range order (SRO) produced by the Br amount. Notably, an increase in SRO within the solid solutions manifests as an emergence of new bands in the Raman spectrum. A redshift in the peaks with increasing Br content in the lattice is observed, which indicates bond stretching in the $[SbCl_{6-\delta}Br_\delta]$ and $[AgCl_{6-\delta}Br_\delta]$ octahedra, in agreement with the XRD data mentioned above. For $\delta = 0$, there are 9 Raman-active modes ($\Gamma_{Raman} = 6F_{2g} + 2E_g + A_g$), with F_{2g} and E_g representing triple and double degenerate vibrational modes, respectively. When $\delta = 1$ or 5, 29 Raman-active ($\Gamma_{Raman} = 7A_1 + 2B_1 + 2B_2 + 18E$) modes can be observed. For $\delta = 2$ or 4, 27 Raman-active modes ($\Gamma_{Raman} = 9A_1 + 4A_2 + 7B_1 + 7B_2$) are reported. For $\delta = 3$, there are 25 Raman-active modes ($\Gamma_{Raman} = 7A_1 + 18E$). At $\delta = 6$, are verified 11 Raman-active modes ($\Gamma_{Raman} = 6E_g + B_{1g} + 2B_{2g} + 2A_{1g}$). The number of Raman-active modes is related to the SRO, with the highest SRO observed for the $Cs_2AgSbCl_3Br_3$ alloy decreasing for $\delta = 2$ or 4, and reaching a minimum for $\delta = 0$ or 6. According to the composition, it is expected that $Cs_2AgSbCl_6$ and $Cs_2AgSbBr_6$ exhibit the same vibrational modes. However, the larger SRO for $Cs_2AgSbBr_6$ arises from the Br^- ions inducing deformation in the octahedral field. This deformation causes almost negligible stretching in the $[AgBr_6]$ and $[SbBr_6]$ polyhedra, resulting in a reduction of SRO and consequent symmetry operations.

The observed distortions in $Cs_2AgSbCl_{6-\delta}Br_\delta$ alloys are intricately related to electronic density redistributions within Ag- and Sb-centered octahedra caused by anion exchange. These distortions lead to the disruption of degeneracy in electronic levels and the emergence of novel electronic states. Figure 4 illustrates the partial DOS (pDOS) for both Ag and Sb atoms in the $[AgCl_{6-\delta}Br_\delta]$ and $[SbCl_{6-\delta}Br_\delta]$ octahedra, respectively. From the pDOS, it becomes evident that anion exchange, depending on the proportion δ (Br amount), i.e., induces diverse orbital degeneracy splittings.

The degeneracy is observed in the t_{1u}, t_{2g}, and e_g orbitals for δ values of 0, 3, and 6, respectively. However, compositions with $\delta = 1$ or 5 exhibit a breakdown in degeneracy, revealing distinct splittings for t_{1u} (e.g., p_y and p_z), t_{2g} (e.g., d_{xz} and d_{xy}), and e_g (e.g., d_{z^2} and $d_{x^2-y^2}$). Similar orbital behavior is reported for $\delta = 2$ or 4, resulting in double degenerate (p_x and p_y) and e (d_{xz} and d_{yz}) orbitals.

Furthermore, in the central atoms (Sb or Ag) of the octahedra, the Ag e_g and t_{2g}, as well as the Sb a_{1u} orbitals, predominantly contribute to the valence band (VB). Conversely, the Sb e_g, t_{2g}, and t_{1u}, along with the Ag a_{1s} and t_{1u} orbitals, make more substantial contributions to the conduction band (CB). Notably, the interval with lower pDOS closer to the VB maximum (VBM) for Ag e_g orbitals indicates higher carrier mobility states, as evidenced by the considerable dispersion of the VBM in the band structures (Figure 5). Similarly, the soft behavior of Sb t_{1u} pDOS in the CB minimum (CBM) signifies higher carrier mobility, corroborated by the pronounced dispersion of the CBM (greater than the VBM).

Upon examining the orbital occupancy for the d-orbital levels of Ag and Sb in $Cs_2AgSbCl_6$, $Cs_2AgSbCl_3Br_3$, and $Cs_2AgSbBr_6$, it becomes evident that the octahedral crystal field splits these levels into triply degenerate t_{2g} (d_{xy}, d_{xz} and d_{yz}) and doubly degenerate e_g (d_{z^2} and $d_{x^2-y^2}$) levels, for both Ag^+ and Sb^{3+} (refer to Table S1 in Supporting Information). Interestingly, the degeneracy of Sb^{3+} d levels is more pronounced than that of Ag^+, with minimal differences in orbital occupancy, particularly in the t_{2g} and e_g orbitals. In the case of Ag^+, a low Jahn−Teller effect (due to the symmetry breaking process) is observed in the t_{2g} and e_g for δ values of 1, 2, 4, and 5, respectively.

Looking at the band structures in Figure 5, a decreasing trend in band gap energy (E_{gap}) is shown with increasing Br concentration. Specifically, the highest and lowest E_{gap} values are found to be 2.72 and 1.77 eV for $Cs_2AgSbCl_6$ and $Cs_2AgSbBr_6$, respectively. It is noticed that the band gap transition remains the same independently of the Br concentration, exhibiting an indirect transition with the VBM at X point and CBM at L point, consistent with previous findings for $Cs_2AgSbCl_{6-\delta}Br_\delta$ compounds.[36] Additionally, a notable dispersion is noticed for the band edges and, consequently, good carrier mobility with the CBM exhibiting a parabolic format. At the Γ point, it is observed that the two highest energy bands of VBM are degenerate for the compositions without splitting the t_{1u}, t_{2g}, and e_g orbitals ($\delta = 0$, 3 and 6). In contrast, this is not observed for the other compositions, corroborating the degeneracy breakdown observed via pDOS. As expected, the reduction of E_{gap} is attributed to the downward movement of the CBM, while the VBM remains practically constant with the Br concentration. Figures 5 and 7 provide a visualization of the E_{gap} as a function of Br concentration, revealing an almost linear decreasing

https://doi.org/10.1021/acs.jpcc.4c01990
J. Phys. Chem. C 2024, 128, 11858−11869

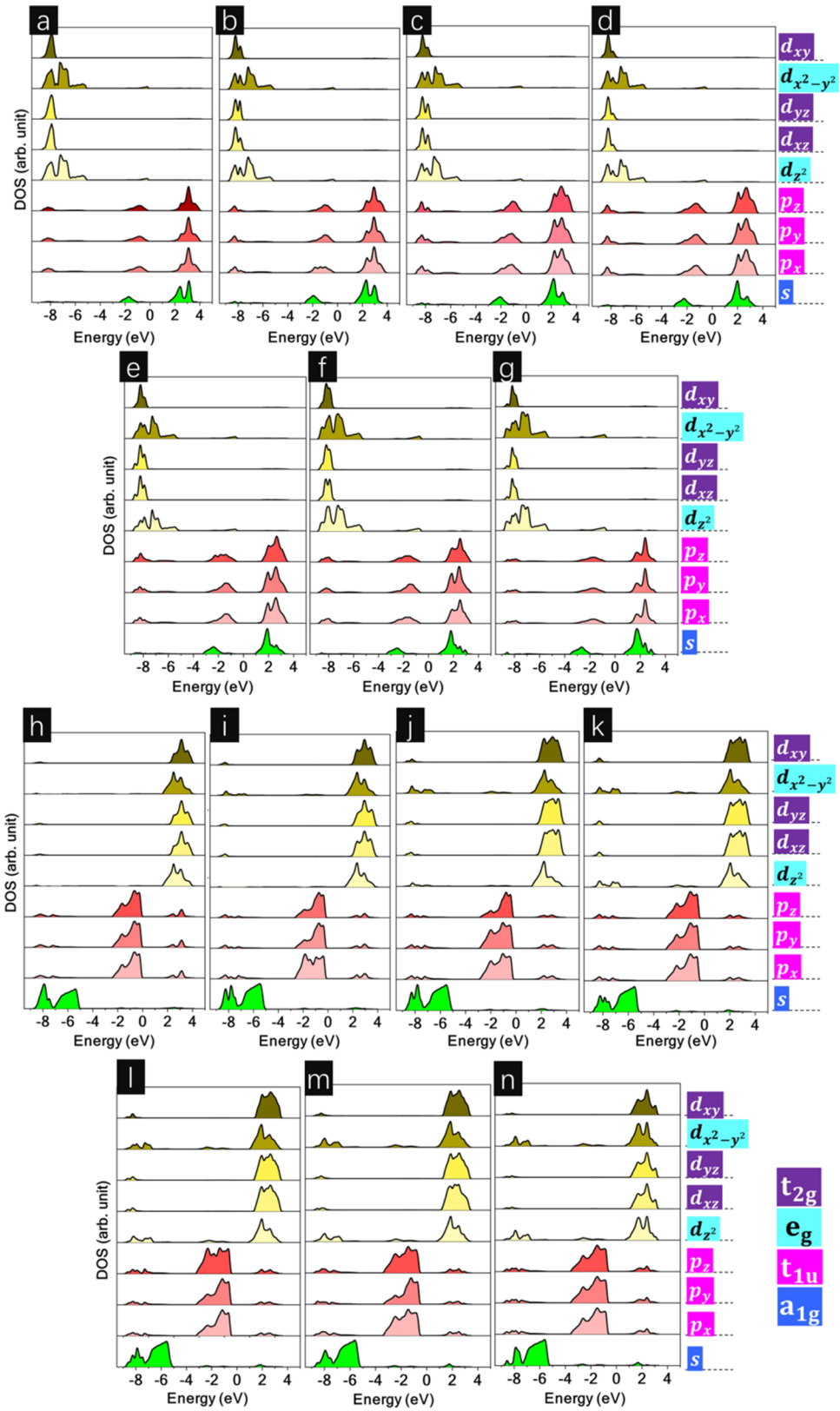

Figure 4. Partial density of states of Ag and Sb in $Cs_2AgSbCl_{6-\delta}Br_\delta$ alloys for $\delta = 0$ (a, h), $\delta = 1$ (b, i), $\delta = 2$ (c, j), $\delta = 3$ (d, k), $\delta = 4$ (e, l), $\delta = 5$ (f, m), and $\delta = 6$ (g, n).

trend. This observation underscores the potential for precise control over the composition of the $Cs_2AgSbCl_{6-\delta}Br_\delta$ matrices. The indirect band gap transition of $Cs_2AgSbCl_{6-\delta}Br_\delta$ can limit its effectiveness in photovoltaic application.[61] However, doping at Sb-site or the design of alloys $Cs_2AgSb_\Delta X_{\Delta-1}Cl_{6-\delta}Br_\delta$, where X is a metal such as In[62] or Tl,[63] can be a strategy to promote the direct band gap transition.

https://doi.org/10.1021/acs.jpcc.4c01990
J. Phys. Chem. C 2024, 128, 11858−11869

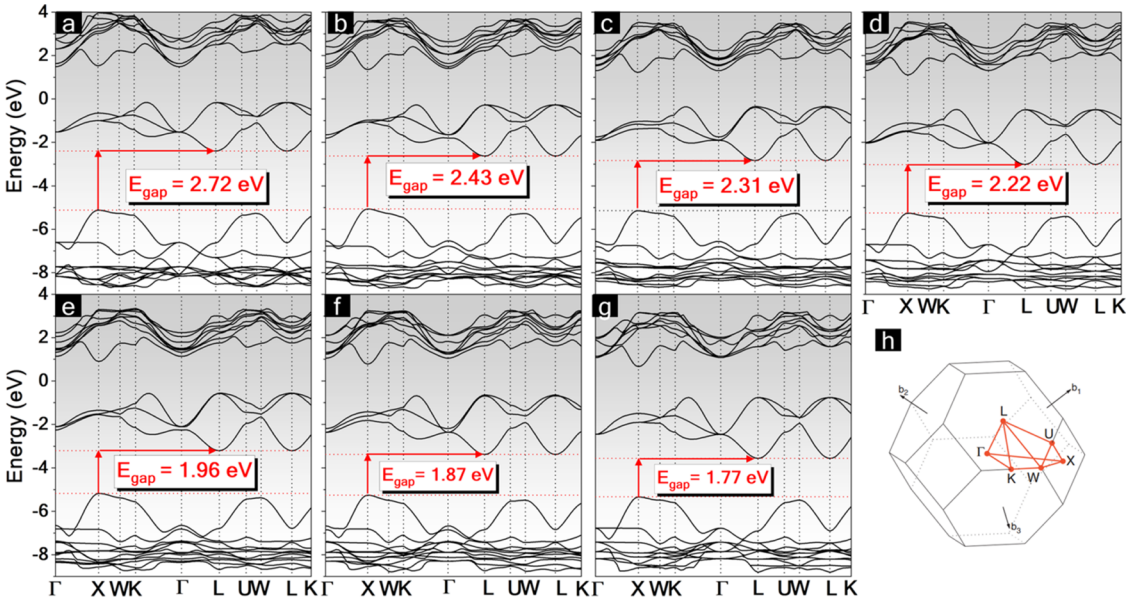

Figure 5. $Cs_2AgSbCl_{6-\delta}Br_\delta$ band structures for $\boldsymbol{\delta}$ = 0 (a), $\boldsymbol{\delta}$ = 1 (b), $\boldsymbol{\delta}$ = 2 (c), $\boldsymbol{\delta}$ = 3 (d), $\boldsymbol{\delta}$ = 4 (e), $\boldsymbol{\delta}$ = 5 (f), and $\boldsymbol{\delta}$ = 6 (g) and the high-symmetry pathway employed along the Brillouin Zone (h).

An electron moving through a crystalline lattice experiences a periodic potential due to the arrangement of atoms in the lattice. This potential arises from the electrostatic interaction between the negatively charged electrons and positively charged atomic nuclei. As the electron moves through the lattice, it interacts with this periodic potential, leading to the concept of an effective mass (m_e^*). When an electron moves along different directions in the lattice, it encounters different strengths of the periodic potential, leading to anisotropic behavior. The concept of effective mass is crucial to understanding the mobility of charge carriers in semiconductors. A lower effective mass means that the electron (or hole) can more easily accelerate in response to an applied electric field, leading to a higher carrier mobility.

In view of this, the effective masses of electrons (m_e^*) and holes (m_h^*) were calculated by fitting a parabolic function to the CBM and VBM, respectively. These parabolic fits were applied in the equation $E = \hbar^2k^2/2m^*$ with a k-point spacing smaller than 0.002 Å^{-1}. Applying the reciprocal effective mass tensor, defined as

$$\left(\frac{1}{m^*}\right)_{\mu\nu} = \frac{1}{\hbar}\frac{d^2E_n(k)}{dk_\mu dk_\nu} \quad (6)$$

where $E_n(k)$ is the nth band energy dispersion, k_μ and k_ν are the K-points in the Brillouin zone in the μ and ν directions, respectively, the m_e^* and m_h^* can be obtained. This approximation considers symmetric paths to obtain a parabolic shape, such as Γ−M−Γ and M−R−M, for example.

To describe the effects of anion-mixing in $Cs_2AgSbCl_{6-\delta}Br_\delta$ systems over m_e^*/m_0 and m_h^*/m_0, these values were presented as functions of Br concentration in Figure 6. In this analysis, the symmetrical pathways in relation to the VBM (Γ−X−Γ) and CBM (L−U−L) were considered to obtain the m_e^*/m_0 and m_h^*/m_0, respectively. The m_e^*/m_0 and m_h^*/m_0 values for all high-symmetry pathways adopted in the band structure plots are present in Table S2 (for more details, see Supporting Information).

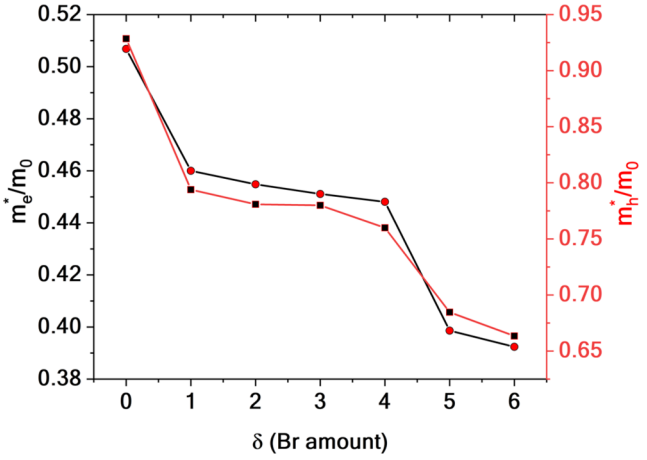

Figure 6. Hole (m_e^*/m_0) and electron (m_h^*/m_0) effective masses obtained on the VBM (Γ−X−Γ pathway) and CBM (L−U−L pathway), respectively, as functions of Br content ($\boldsymbol{\delta}$).

Effective mass values smaller than 0.5 indicate higher carrier mobility, which can be evidenced for m_e^*/m_0 in all systems evaluated ($0.39 < m_e^*/m_0 < 0.51$). On the other hand, the holes exhibit effective masses approximately twice greater than electrons ($0.66 < m_h^*/m_0 < 0.93$). An abrupt decrease for both m_e^*/m_0 and m_h^*/m_0 was perceived with the introduction of one Br ($\boldsymbol{\delta}$ = 1) in the $Cs_2AgSbCl_6$ lattice. After this fall, between $\boldsymbol{\delta}$ = 2 and $\boldsymbol{\delta}$ = 4, the effective masses decrease almost linearly with the $\boldsymbol{\delta}$ increasing. For $\boldsymbol{\delta}$ larger than 4, the behavior becomes irregular; however, it follows the decreasing trend with the Br addition. These results, corroborated by the values in Table S2, unravel that the anion-mixing in these $Cs_2AgSbCl_{6-\delta}Br_\delta$ also can be an effective mechanism to tune the carrier mobility. This higher mobility is essential for efficient charge separation and transport in semiconductor devices such as solar cells, transistors, and sensors.

The elastic behavior of a cubic double halide perovskite is characterized by three independent elastic constants: C_{11}, C_{12}, and C_{44}. Each of these constants plays a distinct role in the

https://doi.org/10.1021/acs.jpcc.4c01990
J. Phys. Chem. C 2024, 128, 11858−11869

material response to external forces and deformation. Specifically, C_{11} describes the material stiffness against the strains, while C_{12} signifies its resistance to shear stress, providing insights into its behavior under lateral forces. Lastly, C_{44} represents the material resistance against shear deformation. Due to the symmetry reduction induced by the anion mixture in the alloys, new independent constants should be considered: for tetragonal systems (δ = 1, 2, 4, 5 or 6), C_{13} and C_{33} are introduced. Similarly, for rhombohedral (δ = 3), C_{13}, C_{14}, and C_{33} are analyzed, in both symmetries, $C_{66} = (C_{11} - C_{12})/2$.

Table 4 shows the calculated elastic constants for all structures. The Born elastic stability criterion was employed to determine the mechanical stability of $Cs_2AgSbCl_{6-\delta}Br_\delta$ alloys for which the necessary and sufficient conditions are[64] $C_{11} - C_{12} > 0$, $C_{11} + 2C_{12} > 0$, and $C_{44} > 0$ for cubic symmetry, $C_{11} > |C_{12}|$, $2(C_{13})^2 < C_{33}(C_{11} + C_{12})$, $C_{44} > 0$, and $C_{66} > 0$ for tetragonal, and $C_{11} > |C_{12}|$; $C_{44} > 0$, $(C_{13})^2 < 1/2(C_{33}(C_{11} + C_{12}))$, and $(C_{14})^2 < 1/2(C_{44}(C_{11} - C_{12})) = C_{44}C_{66}$ for rhombohedral symmetry. It can be concluded that the studied structures exhibit both mechanical and structural stability, meeting the criteria outlined by the Born elastic stability criterion.

Table 4. Calculated Elastic Constants C_{11}, C_{12}, C_{13}, C_{14}, C_{33}, C_{44}, and C_{66} (GPa) for $Cs_2AgSbCl_{6-\delta}Br_\delta$ Compounds

	C_{11}	C_{12}	C_{13}	C_{14}	C_{33}	C_{44}	C_{66}
δ = 0	68.95	24.70				11.55	
δ = 1	69.27	24.14	24.14		65.30	11.78	11.30
δ = 2	66.02	23.64	23.56		62.20	12.00	10.90
δ = 3	62.62	23.23	23.23	−0.05	62.62	11.34	11.34
δ = 4	59.64	22.96	22.45		61.39	11.45	11.48
δ = 5	58.65	23.24	19.88		58.65	11.84	11.84
δ = 6	59.02	20.67	20.67		59.00	10.59	10.59

The mechanical properties of $Cs_2AgSbCl_{6-\delta}Br_\delta$ are comprehensively summarized in Table 5, encompassing essential parameters such as the bulk modulus (K), Young modulus (Y), Poisson ratio (ν), and shear modulus (G). These parameters offer insights into the material's response to various mechanical stresses and deformations. In particular, the K describes the material resistance to compression or volume reduction, and Y characterizes its stiffness against tensile or compressive forces. Poisson ratio, ν, describes the material deformation behavior—whether it tends to expand or contract laterally when subjected to axial stress. The G quantifies a material resistance to deformation under shear stress, providing insights into its structural integrity.[65] Utilizing the Voigt averaging scheme, average values of these properties (K_{av}, Y_{av}, and ν_{av}) are computed, alongside presenting the maximum and minimum values for each parameter (Y_{max}, Y_{min}, ν_{max}, ν_{min}, G_{max}, and G_{min}) in order to assess anisotropy.

Upon introduction of Br into the system, both $K_{a\nu}$ and $Y_{a\nu}$ exhibit a noteworthy decrease. Intriguingly, this reduction follows an almost linear trend concerning Br concentration, as illustrated in Figure 7a. The linear fittings underscore the possibility of accurately describing these relationships with two linear expressions, supported by R^2 values approaching 1. Notably, $K_{a\nu}$ experiences a slightly more pronounced decrease than $Y_{a\nu}$.

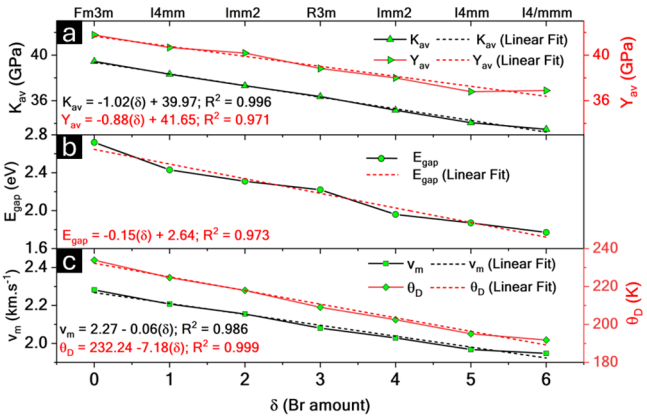

Figure 7. Bulk modulus (K_{av}) and Young modulus (Y_{av}) average values in GPa (a), Band gap energy (E_{gap}) (b) and sound velocity (v_m) and Debye temperature (θ_D) (c) as functions of the Br concentration (δ) and their respective linear fittings.

In contrast, Poisson ratio ($\nu_{a\nu}$) and the shear modulus ($G_{a\nu}$) demonstrate practical independence from Br concentration, showing minimal variations. For $\delta \neq 0$ and 6, the anisotropy in Y is lower compared to pure compounds (δ = 0 or 6) and diminishes with increasing Br concentration. Maximum and minimum values of ν and G remain nearly constant, unaffected by the Br concentration. Among the mechanical properties evaluated, the highest anisotropy is observed for ν.

The Debye temperature (θ_D) represents the temperature at which the highest frequency vibration mode (and consequently, all modes) is excited in a crystal.[66,67] From this perspective, the Debye temperature acts as a divider between the high- and low-temperature regions of a solid, being particularly useful for the study of thermal phenomena and properties (e.g., thermal conductivity, lattice vibration, specific heat, and volume thermal expansion coefficient). When the temperature T of a solid is raised above θ_D, it is expected that each vibration mode is associated with an energy equal to k_BT.

Table 5. Average, Maximum, and Minimum Values of Bulk Modulus (K_{av}, K_{max}, and K_{min}), Young Modulus (Y_{av}, Y_{max}, and Y_{min}), Poisson Ratio (ν_{av}, ν_{max}, and ν_{min}), and Shear Modulus (G_{av}, G_{max}, and G_{min}). K, Y, and G are in GPa, and the Average Values were Obtained Using the Voigt Averaging Scheme

	K_{av}	Y_{av}	ν_{av}	G_{av}	Y_{max}	Y_{min}	ν_{max}	ν_{min}	G_{max}	G_{min}
δ = 0	39.45	41.77	0.32	15.78	55.92	31.56	0.53	0.17	22.12	11.55
δ = 1	38.32	40.67	0.32	15.36	56.25	31.25	0.53	0.17	21.54	11.30
δ = 2	37.31	40.18	0.32	15.21	53.30	31.37	0.54	0.18	21.19	10.90
δ = 3	36.36	38.83	0.32	14.68	50.05	30.40	0.51	0.18	19.70	11.24
δ = 4	35.16	38.00	0.32	14.40	49.18	30.87	0.48	0.20	19.02	11.36
δ = 5	34.06	36.79	0.32	13.93	46.92	30.01	0.49	0.19	19.39	10.20
δ = 6	33.48	36.89	0.32	14.01	48.32	28.74	0.51	0.17	19.17	10.58

https://doi.org/10.1021/acs.jpcc.4c01990
J. Phys. Chem. C 2024, 128, 11858−11869

At $T < \theta_D$, all high-frequency modes are suspended, with vibrational excitations due to acoustic vibrations. Here, the Anderson method was used to determine the Debye temperature (θ_D). The Debye temperature is determined from the following equation:[68,69]

$$\theta_D = \frac{h}{k_B}\left[\frac{(3n/4\pi)N_A\rho}{M}\right]^{1/3} v_m \quad (7)$$

where v_m is the average sound velocity, h is Planck's constant, k_B is Boltzmann constant, n is the number of atoms per unit cell, N_A is Avogadro's number, ρ is the mass density, and M is the molecular weight. The v_m within a material is obtained by

$$v_m = \left[\frac{1}{3}\left(\frac{2}{v_t^3} + \frac{1}{v_l^3}\right)\right]^{-1/3} \quad (8)$$

where v_t and v_l represent the transverse and longitudinal sound velocities, respectively. These velocities can be estimated by using Navier's equations:

$$v_l = \left(\frac{3B + 4G}{3\rho}\right)^{1/2} \quad (9)$$

$$v_t = \left(\frac{G}{\rho}\right)^{1/2} \quad (10)$$

Figure 7c shows the calculated θ_D and v_m as functions of the $\boldsymbol{\delta}$ for $Cs_2AgSbCl_{6-\delta}Br_\delta$ alloys. Increasing $\boldsymbol{\delta}$, i.e., the Br concentration, the Debye temperature decreases linearly. Low θ_D values indicate lower interatomic forces and weak bonds. This can be evidenced by Table 4, where it is noticed that the elastic constants decrease with increasing $\boldsymbol{\delta}$. Also, it can be observed that the sound velocity (v_m) decreases linearly with an increase in Br concentration. A lower thermal conductivity leads to a lower Debye temperature, which is suitable for thermoelectric applications. Similar behavior was reported for Cs_2AgSbX_6 (X = Cl, Br, and I),[70] revealing that most soft anions lead to a reduction in the θ_D and v_m, explaining the reduction of these parameters with the Br addition.

4. CONCLUSIONS

This computational study investigated the lead-free $Cs_2AgSbCl_{6-\delta}Br_\delta$ mixed-halide double perovskites, including lattice parameters, band structures, density of states, XRD patterns, vibrational frequencies, and mechanical properties, using DFT/PBESOL0 calculations.

The structural stability of various perovskite materials was assessed through the analysis of tolerance factors such as Goldschmidt and Bartel. According to Goldschmit factor, all perovskites can be considered stable. In contrast, Bartel factor demonstrates that the stability is guaranteed only for $\boldsymbol{\delta}$ = 0, 1, and 2, which represents a remarkable difference between these two very utilized parameters. However, the two indicate that Br increases the instability in $Cs_2AgSbCl_{6-\delta}Br_\delta$ systems.

The short-range order was investigated via Raman spectroscopy. As Br content increased, an increase in short-range order was verified, leading to the emergence of new bands, accompanied by a red shift in peaks. Different δ values correspond to varying numbers of Raman-active modes: 9 modes for δ = 0, 29 modes for δ = 1 or 5, 27 modes for δ = 2 or 4, 25 modes for δ = 3, and 11 modes for δ = 6. This red shift is related to bond stretching in the $[SbCl_{6-\delta}Br_\delta]$ and $[AgCl_{6-\delta}Br_\delta]$ octahedra, consistent with simulated X-ray diffraction patterns.

The incorporation of Br atoms leads to a reduction in the band gap energy of $Cs_2AgSbCl_{6-\delta}Br_\delta$ from 2.72 to 1.77 eV. All structures exhibit indirect X → L band gap transitions. The observed reductions in bulk modulus and Young modulus with increasing Br concentration highlight the influence of anion exchange on mechanical behavior.

Furthermore, the linear decrease in Debye temperature and average sound velocity as Br concentration increases suggests weaker interatomic forces and bonds within the alloys. This finding has significant implications for applications requiring low thermal conductivity such as thermoelectric materials. Finally, from this perspective, we demonstrate the tunability of structural and electronic properties through halide substitution, highlighting the potential of the $Cs_2AgSbCl_{6-\delta}Br_\delta$ system as a versatile lead-free platform for emerging optoelectronic applications.

■ ASSOCIATED CONTENT

Supporting Information

The Supporting Information is available free of charge at https://pubs.acs.org/doi/10.1021/acs.jpcc.4c01990.

Orbital occupancy on Ag and Sb atoms in $[AgCl_{6-\delta}Br_\delta]$ and $[SbCl_{6-\delta}Br_\delta]$ octahedra for $Cs_2AgSbCl_{6-\delta}Br_\delta$ alloys; electron and hole effective masses and m_h/m_e ratio for all high-symmetry pathways along the Brillouin Zone for $Cs_2AgSbCl_{6-\delta}Br_\delta$ alloys (PDF)

■ AUTHOR INFORMATION

Corresponding Author

Julio R. Sambrano − *Modeling and Molecular Simulation Group, São Paulo State University, 17033-360 Bauru, SP, Brazil;* orcid.org/0000-0002-5217-7145; Email: jr.sambrano@unesp.br

Authors

José A. S. Laranjeira − *Modeling and Molecular Simulation Group, São Paulo State University, 17033-360 Bauru, SP, Brazil;* orcid.org/0000-0002-8366-7227

Sérgio A. Azevedo − *Federal Institute of Maranhão, 65950-000 Barra do Corda, Ma, Brazil; Maranhense Center College − FCMA/UNICENTRO, 65950-000 Barra do Corda, MA, Brazil;* orcid.org/0000-0002-5289-4101

Felipe A. La Porta − *Nanotechnology and Computational Chemistry Laboratory, Federal University of Technology—Paraná, 86036-370 Londrina, PR, Brazil; Post-Graduation Program in Chemistry, State University of Londrina, 86057-970 Londrina, PR, Brazil;* orcid.org/0000-0003-0990-7947

Mateus M. Ferrer − *Postgraduate Program in Materials Science and Engineering, Federal University of Pelotas, 96010-610 Pelotas, RS, Brazil*

Elson Longo − *CDMF, Federal University of São Carlos, 14801-907 São Carlos, SP, Brazil;* orcid.org/0000-0001-8062-7791

Complete contact information is available at: https://pubs.acs.org/10.1021/acs.jpcc.4c01990

Funding

The Article Processing Charge for the publication of this research was funded by the Coordination for the Improvement of Higher Education Personnel - CAPES (ROR identifier: 00x0ma614).

Notes

The authors declare no competing financial interest.

■ ACKNOWLEDGMENTS

This work was supported by the Brazilian funding agencies Fundação de Amparo à Pesquisa do Estado de São Paulo—FAPESP (grant nos. 22/03959-6, 22/16509-9, and 20/01144-0), Fundação de Amparo à Pesquisa do Estado do Rio Grande do Sul—FAPERGS (grant no. 23/2551-0000153-5), National Council for Scientific and Technological Development—CNPq (grant nos. 307213/2021-8 and 150187/2023-8), and Coordination for the Improvement of Higher Education Personnel (grant no. 88887.827928/2023-00). The computational facilities were supported by resources supplied by the Molecular Simulations Laboratory (São Paulo State University, Bauru, Brazil).

■ REFERENCES

(1) Dong, C. R.; Wang, Y.; Zhang, K.; Zeng, H. Halide Perovskite Materials as Light Harvesters for Solar Energy Conversion. *Energy Chem.* **2020**, *2* (1), No. 100026.

(2) Castelli, I. E.; Hüser, F.; Pandey, M.; Li, H.; Thygesen, K. S.; Seger, B.; Jain, A.; Persson, K. A.; Ceder, G.; Jacobsen, K. W. New Light-Harvesting Materials Using Accurate and Efficient Bandgap Calculations. *Adv. Energy Mater.* **2015**, *5* (2), No. 1400915.

(3) Cai, Y.; Xie, W.; Ding, H.; Chen, Y.; Thirumal, K.; Wong, L. H.; Mathews, N.; Mhaisalkar, S. G.; Sherburne, M.; Asta, M. Computational Study of Halide Perovskite-Derived A2BX6 Inorganic Compounds: Chemical Trends in Electronic Structure and Structural Stability. *Chem. Mater.* **2017**, *29* (18), 7740−7749.

(4) Ghasemi, M.; Hao, M.; Xiao, M.; Chen, P.; He, D.; Zhang, Y.; Chen, W.; Fan, J.; Yun, J. H.; Jia, B.; Wen, X. Lead-Free Metal-Halide Double Perovskites: From Optoelectronic Properties to Applications. *Nanophotonics* **2021**, *10* (8), 2181−2219.

(5) Noel, N. K.; Stranks, S. D.; Abate, A.; Wehrenfennig, C.; Guarnera, S.; Haghighirad, A. A.; Sadhanala, A.; Eperon, G. E.; Pathak, S. K.; Johnston, M. B.; et al. Lead-Free Organic−Inorganic Tin Halide Perovskites for Photovoltaic Applications. *Energy Environ. Sci.* **2014**, *7* (9), 3061−3068.

(6) Chen, D.; Ba, Y.; Deng, M.; Zhu, W.; Chai, W.; Xi, H.; Chen, D.; Zhang, J.; Zhang, C.; Hao, Y. High-Purity, Thick CsPbCl3 Films toward Selective Ultraviolet-Harvesting Visibly Transparent Photovoltaics. *ACS Appl. Energy Mater.* **2021**, *4* (11), 12121−12127.

(7) Tang, Y.; Lesage, A.; Schall, P. CsPbI3 Nanocrystal Films: Towards Higher Stability and Efficiency. *J. Mater. Chem. C* **2020**, *8* (48), 17139−17156.

(8) Zhang, S.; Liu, H.; Li, X.; Wang, S. Enhancing Quantum Yield of CsPb(BrxCl1-x)3 Nanocrystals through Lanthanum Doping for Efficient Blue Light-Emitting Diodes. *Nano Energy* **2020**, *77*, No. 105302.

(9) Best Research-Cell Efficiency Chart|Photovoltaic Research| NREL. https://www.nrel.gov/pv/cell-efficiency.html (accessed May 30, 2023).

(10) Green, M.; Dunlop, E.; Hohl-Ebinger, J.; Yoshita, M.; Kopidakis, N.; Hao, X. Solar Cell Efficiency Tables (Version 57). *Prog. Photovoltaics: Res. Appl.* **2021**, *29* (1), 3−15.

(11) Akkerman, Q. A.; Manna, L. What Defines a Halide Perovskite? *ACS Energy Lett.* **2020**, *5* (2), 604−610.

(12) Manser, J. S.; Christians, J. A.; Kamat, P. V. Intriguing Optoelectronic Properties of Metal Halide Perovskites. *Chem. Rev.* **2016**, *116* (21), 12956−13008.

(13) Liu, D.; Peng, H.; Li, Q.; Sa, R. A DFT Study of the Stability and Optoelectronic Properties of All-Inorganic Lead-Free Halide Perovskites. *J. Phys. Chem. Solids* **2022**, *161*, No. 110413.

(14) Huang, L. Y.; Lambrecht, W. R. L. Electronic Band Structure Trends of Perovskite Halides: Beyond Pb and Sn to Ge and Si. *Phys. Rev. B* **2016**, *93* (19), No. 195211.

(15) Dou, J.; Bai, Y.; Chen, Q. Challenges of Lead Leakage in Perovskite Solar Cells. *Mater. Chem. Front.* **2022**, *6* (19), 2779−2789.

(16) Zhao, S.; Yamamoto, K.; Iikubo, S.; Hayase, S.; Ma, T. First-Principles Study of Electronic and Optical Properties of Lead-Free Double Perovskites Cs2NaBX6 (B = Sb, Bi; X = Cl, Br, I). *J. Phys. Chem. Solids* **2018**, *117*, 117−121.

(17) McClure, E. T.; Ball, M. R.; Windl, W.; Woodward, P. M. Cs2AgBiX6 (X = Br, Cl): New Visible Light Absorbing, Lead-Free Halide Perovskite Semiconductors. *Chem. Mater.* **2016**, *28* (5), 1348−1354.

(18) Zhang, L.; Fang, Y.; Sui, L.; Yan, J.; Wang, K.; Yuan, K.; Mao, W. L.; Zou, B. Tuning Emission and Electron-Phonon Coupling in Lead-Free Halide Double Perovskite Cs2AgBiCl6 under Pressure. *ACS Energy Lett.* **2019**, *4* (12), 2975−2982.

(19) Zhou, J.; Rong, X.; Molokeev, M. S.; Zhang, X.; Xia, Z. Exploring the Transposition Effects on the Electronic and Optical Properties of Cs2AgSbCl6via a Combined Computational-Experimental Approach. *J. Mater. Chem. A* **2018**, *6* (5), 2346−2352.

(20) Shadabroo, M. S.; Abdizadeh, H.; Golobostanfard, M. R. Elpasolite Structures Based on A2AgBiX6 (A: MA, Cs, X: I, Br): Application in Double Perovskite Solar Cells. *Mater. Sci. Semicond. Process.* **2021**, *125*, No. 105639.

(21) Pinto, F. M.; de Conti, M. C. M. D.; Dey, S.; Velilla, E.; Taft, C. A.; de Almeida La Porta, F. Emerging Metal-Halide Perovskite Materials for Enhanced Solar Cells and Light-Emitting Applications. *Eng. Mater.* **2022**, 45−85.

(22) Liu, Y.; Nag, A.; Manna, L.; Xia, Z. Lead-Free Double Perovskite Cs2AgInCl6. *Angew. Chem., Int. Ed.* **2021**, *60* (21), 11592−11603.

(23) García-Espejo, G.; Rodríguez-Padrón, D.; Luque, R.; Camacho, L.; De Miguel, G. Mechanochemical Synthesis of Three Double Perovskites: Cs2AgBiBr6, (CH3NH3)2TlBiBr6 and Cs2AgSbBr6. *Nanoscale* **2019**, *11* (35), 16650−16657.

(24) Wu, C.; Zhang, Q.; Liu, Y.; Luo, W.; Guo, X.; Huang, Z.; Ting, H.; Sun, W.; Zhong, X.; Wei, S.; et al. The Dawn of Lead-Free Perovskite Solar Cell: Highly Stable Double Perovskite Cs2AgBiBr6 Film. *Adv. Sci.* **2018**, *5* (3), No. 1700759.

(25) Dahl, J. C.; Osowiecki, W. T.; Cai, Y.; Swabeck, J. K.; Bekenstein, Y.; Asta, M.; Chan, E. M.; Alivisatos, A. P. Probing the Stability and Band Gaps of Cs2AgInCl6 and Cs2AgSbCl6 Lead-Free Double Perovskite Nanocrystals. *Chem. Mater.* **2019**, *31* (9), 3134−3143.

(26) McClure, E. T.; Ball, M. R.; Windl, W.; Woodward, P. M. Cs2AgBiX6 (X = Br, Cl): New Visible Light Absorbing, Lead-Free Halide Perovskite Semiconductors. *Chem. Mater.* **2016**, *28* (5), 1348−1354.

(27) Zhou, J.; Rong, X.; Molokeev, M. S.; Zhang, X.; Xia, Z. Exploring the Transposition Effects on the Electronic and Optical Properties of Cs2AgSbCl 6 via a Combined Computational-Experimental Approach. *J. Mater. Chem. A* **2018**, *6* (5), 2346−2352.

(28) Deng, W.; Deng, Z. Y.; He, J.; Wang, M.; Chen, Z. X.; Wei, S. H.; Feng, H. J. Synthesis of Cs2AgSbCl6 and Improved Optoelectronic Properties of Cs2AgSbCl6/TiO2 Heterostructure Driven by the Interface Effect for Lead-Free Double Perovskites Solar Cells. *Appl. Phys. Lett.* **2017**, *111*, No. 151602, DOI: 10.1063/1.4999192/34133.

(29) Yu, G.; Xue, S.; Yin, R.; Wu, Q.; Gao, T.; Song, Y.; Wang, R.; Cong, W. Y.; Guan, C. B.; Lu, Y. B. How the Copper Dopant Alters the Geometric and Photoelectronic Properties of the Lead-Free Cs2AgSbCl6 Double Perovskite. *Adv. Theory Simul.* **2021**, *4* (8), No. 2100142.

(30) Sandeep, K.; Padmakumar, K.; Ambili, K. U.; Jishnu, P.; Fousia, K. H.; Ramesh, A. R.; Rappai, J. P.; Santhi, V.; Shanthil, M. Anion

Exchange in Lead Halide Perovskites: An Overview. *Phys. Status Solidi B* **2022**, *259* (4), No. 2100600.
(31) Ono, L. K.; Juarez-Perez, E. J.; Qi, Y. Progress on Perovskite Materials and Solar Cells with Mixed Cations and Halide Anions. *ACS Appl. Mater. Interfaces* **2017**, *9* (36), 30197−30246.
(32) Rehman, W.; Milot, R. L.; Eperon, G. E.; Wehrenfennig, C.; Boland, J. L.; Snaith, H. J.; Johnston, M. B.; Herz, L. M.; Rehman, W.; Milot, R. L.; Eperon, G. E.; et al. Charge-Carrier Dynamics and Mobilities in Formamidinium Lead Mixed-Halide Perovskites. *Adv. Mater.* **2015**, *27* (48), 7938−7944.
(33) Brennan, M. C.; Draguta, S.; Kamat, P. V.; Kuno, M. Light-Induced Anion Phase Segregation in Mixed Halide Perovskites. *ACS Energy Lett.* **2018**, *3* (1), 204−213.
(34) Akkerman, Q. A.; D'Innocenzo, V.; Accornero, S.; Scarpellini, A.; Petrozza, A.; Prato, M.; Manna, L. Tuning the Optical Properties of Cesium Lead Halide Perovskite Nanocrystals by Anion Exchange Reactions. *J. Am. Chem. Soc.* **2015**, *137* (32), 10276−10281.
(35) Wu, H.; Erbing, A.; Johansson, M. B.; Wang, J.; Kamal, C.; Odelius, M.; Johansson, E. M. J. Mixed-Halide Double Perovskite Cs2AgBiX6 (X = Br, I) with Tunable Optical Properties via Anion Exchange. *ChemSusChem* **2021**, *14* (20), 4507−4515.
(36) Su, J.; Mou, T.; Wen, J.; Wang, B. First-Principles Study on the Structure, Electronic, and Optical Properties of Cs2AgBiBr6-XClx Mixed-Halide Double Perovskites. *J. Phys. Chem. C* **2020**, *124* (9), 5371−5377.
(37) Chapa, W. A.; Wanniarachchi, P.; Eidsvåg, H.; Arunasalam, T.; Ravirajan, P.; Velauthapillai, D.; Vajeeston, P. Deep Insight into Structural and Optoelectronic Properties of Mixed Anion Perovskites. *Mater. Res. Express* **2024**, *11*, No. 025901.
(38) Dovesi, R.; Orlando, R.; Civalleri, B.; Roetti, C.; Saunders, V. R.; Zicovich-Wilson, C. M. CRYSTAL: A Computational Tool for the Ab Initio Study of the Electronic Properties of Crystals. *Z. Kristallogr. - Cryst. Mater.* **2005**, *220* (5−6), 571−573.
(39) Adamo, C.; Barone, V. Toward Reliable Density Functional Methods without Adjustable Parameters: The PBE0Model. *J. Chem. Phys.* **1999**, *110* (13), 6158−6170.
(40) Vilela Oliveira, D.; Laun, J.; Peintinger, M. F.; Bredow, T. BSSE-Correction Scheme for Consistent Gaussian Basis Sets of Double- and Triple-Zeta Valence with Polarization Quality for Solid-State Calculations. *J. Comput. Chem.* **2019**, *40* (27), 2364−2376.
(41) Momma, K.; Izumi, F. VESTA: A Three-Dimensional Visualization System for Electronic and Structural Analysis. *J. Appl. Crystallogr.* **2008**, *41* (3), 653−658, DOI: 10.1107/S0021889808012016.
(42) Zhou, J.; Rong, X.; Molokeev, M. S.; Zhang, X.; Xia, Z. Exploring the Transposition Effects on the Electronic and Optical Properties of Cs2AgSbCl6 via a Combined Computational-Experimental Approach. *J. Mater. Chem. A* **2018**, *6* (5), 2346−2352.
(43) Tran, T. T.; Panella, J. R.; Chamorro, J. R.; Morey, J. R.; McQueen, T. M. Designing Indirect−Direct Bandgap Transitions in Double Perovskites. *Mater. Horiz.* **2017**, *4* (4), 688−693.
(44) Karmakar, A.; Dodd, M. S.; Agnihotri, S.; Ravera, E.; Michaelis, V. K. Cu(II)-Doped Cs2SbAgCl6 Double Perovskite: A Lead-Free, Low-Bandgap Material. *Chem. Mater.* **2018**, *30* (22), 8280−8290.
(45) Rodrigues, J. E. F. S.; Escanhoela, C. A.; Fragoso, B.; Sombrio, G.; Ferrer, M. M.; Álvarez-Galván, C.; Fernández-Díaz, M. T.; Souza, J. A.; Ferreira, F. F.; Pecharromán, C.; Alonso, J. A. Experimental and Theoretical Investigations on the Structural, Electronic, and Vibrational Properties of Cs2AgSbCl6 Double Perovskite. *Ind. Eng. Chem. Res.* **2021**, *60* (51), 18918−18928.
(46) Ornelas-Cruz, I.; Trejo, A.; Oviedo-Roa, R.; Salazar, F.; Carvajal, E.; Miranda, A.; Cruz-Irisson, M. DFT-Based Study of the Bulk Tin Mixed-Halide CsSnI3-XBrx Perovskite. *Comput. Mater. Sci.* **2020**, *178*, No. 109619.
(47) González, I.; Sosa, A. N.; Trejo, A.; Calvino, M.; Miranda, A.; Cruz-Irisson, M. Lithium Effect on the Electronic Properties of Porous Silicon for Energy Storage Applications: A DFT Study. *Dalton Trans.* **2018**, *47* (22), 7505−7514.
(48) Dos Santos, R. M.; Ornelas-Cruz, I.; Dias, A. C.; Lima, M. P.; Da Silva, J. L. F. Theoretical Investigation of the Role of Mixed A +Cations in the Structure, Stability, and Electronic Properties of Perovskite Alloys. *ACS Appl. Energy Mater.* **2023**, *6* (10), 5259−5273.
(49) Lee, J. H.; Bristowe, N. C.; Lee, J. H.; Lee, S. H.; Bristowe, P. D.; Cheetham, A. K.; Jang, H. M. Resolving the Physical Origin of Octahedral Tilting in Halide Perovskites. *Chem. Mater.* **2016**, *28* (12), 4259−4266.
(50) Wei, F.; Deng, Z.; Sun, S.; Hartono, N. T. P.; Seng, H. L.; Buonassisi, T.; Bristowe, P. D.; Cheetham, A. K. Enhanced Visible Light Absorption for Lead-Free Double Perovskite Cs2AgSbBr6. *Chem. Commun.* **2019**, *55* (26), 3721−3724.
(51) Adhikari, S.; Johari, P. Theoretical Insights into Monovalent-Metal-Cation Transmutation Effects on Lead-Free Halide Double Perovskites for Optoelectronic Applications. *Phys. Rev. Mater.* **2023**, *7* (7), No. 075401.
(52) Siddique, Z.; Payne, J. L.; Irvine, J. T. S.; Jagadamma, L. K.; Akhter, Z.; Samuel, I. D. W.; Iqbal, A. Effect of Halide-Mixing on Tolerance Factor and Charge-Carrier Dynamics in (CH3 NH3 PbBr3−x Clx) Perovskites Powders. *J. Mater. Sci.: Mater. Electron.* **2020**, *31* (21), 19415−19428.
(53) Li, C.; Soh, K. C. K.; Wu, P. Formability of ABO3 Perovskites. *J. Alloys Compd.* **2004**, *372* (1−2), 40−48.
(54) Shannon, R. D. Revised Effective Ionic Radii and Systematic Studies of Interatomic Distances in Halides and Chalcogenides. *Acta Crystallogr.* **1976**, *32* (5), 751−767, DOI: 10.1107/S0567739476001551.
(55) Bartel, C. J.; Sutton, C.; Goldsmith, B. R.; Ouyang, R.; Musgrave, C. B.; Ghiringhelli, L. M.; Scheffler, M. New Tolerance Factor to Predict the Stability of Perovskite Oxides and Halides. *Sci. Adv.* **2019**, *5* (2), No. eaav0693.
(56) Hoppe, R. Effective Coordination Numbers (ECoN) and Mean Fictive Ionic Radii (MEFIR). *Z. Kristallogr. - Cryst. Mater.* **1979**, *150* (1−4), 23−52.
(57) Laranjeira, J. A. S.; Azevedo, S. A.; Fabris, G. S. L.; Albuquerque, A. R.; Ferrer, M. M.; Sambrano, J. R. Surface-Dependent Properties and Morphological Transformations of Rutile GeO2 Nanoparticles. *Appl. Surf. Sci.* **2023**, *609*, No. 155321.
(58) Laranjeira, J. A. S.; Fabris, G. S. L.; Albuquerque, A. R.; Ferrer, M. M.; Sambrano, J. R. Morphological Transformations Mapping of CaXO4 (X = Mo or W) and Their Surface Stability. *Mater. Today Commun.* **2022**, *33*, No. 104178, DOI: 10.1016/j.mtcomm.2022.104178.
(59) Laranjeira, J. A. S.; Azevedo, S. A.; Fabris, G. S. L.; Albuquerque, A. R.; Ferrer, M. M.; Sambrano, J. R. Influence of Anion Hardness in (001) Surface of CsPbX3 (X = F, Cl, Br and I) Halide Perovskites. *J. Solid State Chem.* **2023**, *326*, No. 124181.
(60) Guinier, A. *X-Ray Diffraction in Crystals, Imperfect Crystals, and Amorphous Bodies*; Courier Corporation, 1994.
(61) Yu, C. J.; Ri, I. C.; Ri, H. M.; Jang, J. H.; Kim, Y. S.; Jong, U. G. First-Principles Study on Structural, Electronic and Optical Properties of Halide Double Perovskite Cs2AgBX6 (B = In, Sb; X = F, Cl, Br, I). *RSC Adv.* **2023**, *13* (23), 16012−16022.
(62) Chen, L.; Jiang, H.; Luo, Z.; Liu, G.; Wu, X.; Liu, Y.; Sun, P.; Jiang, J. Enhancement of the Efficiency and Thermal Stability of the Double Perovskite Cs2AgInCl6 Single Crystal by Sc Substitution. *Mater. Adv.* **2022**, *3* (10), 4381−4386.
(63) Slavney, A. H.; Leppert, L.; Bartesaghi, D.; Gold-Parker, A.; Toney, M. F.; Savenije, T. J.; Neaton, J. B.; Karunadasa, H. I. Defect-Induced Band-Edge Reconstruction of a Bismuth-Halide Double Perovskite for Visible-Light Absorption. *J. Am. Chem. Soc.* **2017**, *139* (14), 5015−5018.
(64) Mouhat, F.; Coudert, F. X. Necessary and Sufficient Elastic Stability Conditions in Various Crystal Systems. *Phys. Rev. B* **2014**, *90* (22), No. 224104.
(65) Zosiamliana, R.; Chettri, B.; Fabris, G. S. L.; Sambrano, J. R.; Abdullaev, S.; Abdurakhmanov, G.; Rai, D. P. Electronic, Mechanical and Piezoelectric Properties of Glass-like Complex Na2Si1−xGexO3

(x = 0.0, 0.25, 0.50, 0.75, 1.0). *RSC Adv.* **2022**, *12* (42), 27666−27678.
(66) Steven, H. S. *The Oxford Solid State Basics*; Oxford, 2013.
(67) Pecinatto, H.; Mota, C.; Frota, H. O. Determination of the Mechanical, Thermal, Electronic and Optoelectronics Properties of BaMoO4 with Oxygen Vacancy by Ab-Initio Calculations. *Mater. Today Commun.* **2023**, *34*, No. 105074.
(68) Ahmad Khandy, S.; Islam, I.; Kaur, K.; Laref, A.; Dhiman, S.; Rubab, S.; Gupta, D. C.; Khenata, R. DFT Investigations on the Electronic Structure, Magnetism, Thermodynamic and Elastic Properties of Newly Predicted Cobalt Based Antiperovskites: Co3XN (X = Pd, Pt & Rh). *Results Phys.* **2020**, *17*, No. 103112.
(69) Anderson, O. L. A Simplified Method for Calculating the Debye Temperature from Elastic Constants. *J. Phys. Chem. Solids* **1963**, *24* (7), 909−917.
(70) Babaei, M.; Ahmadi, V.; Darvish, G. Opto-Electro-Mechanical Properties of Lead-Free Hybrid Double Perovskites Cs2AgSbX6 (X = Cl, Br, I) for Solar Cells: A First-Principles Study. *J. Phys. Chem. Solids* **2022**, *169*, No. 110880.

https://doi.org/10.1021/acs.jpcc.4c01990
J. Phys. Chem. C 2024, 128, 11858−11869